YALE PEABODY MUSEUM

JOURNAL OF MARINE RESEARCH

The *Journal of Marine Research,* one of the oldest journals in American marine science, published important peer-reviewed original research on a broad array of topics in physical, biological, and chemical oceanography vital to the academic oceanographic community in the long and rich tradition of the Sears Foundation for Marine Research at Yale University.

An archive of all issues from 1937 to 2021 (Volume 1–79) are available through EliScholar, a digital platform for scholarly publishing provided by Yale University Library at https://elischolar.library.yale.edu/.

Requests for permission to clear rights for use of this content should be directed to the authors, their estates, or other representatives. The *Journal of Marine Research* has no contact information beyond the affiliations listed in the published articles. We ask that you provide attribution to the *Journal of Marine Research.*

Yale University provides access to these materials for educational and research purposes only. Copyright or other proprietary rights to content contained in this document may be held by individuals or entities other than, or in addition to, Yale University. You are solely responsible for determining the ownership of the copyright, and for obtaining permission for your intended use. Yale University makes no warranty that your distribution, reproduction, or other use of these materials will not infringe the rights of third parties.

Journal of
MARINE RESEARCH

On the amplification of convergences in coastal currents and the formation of "squirts"

by Melvin E. Stern[1]

ABSTRACT

We consider the temporal evolution of a slow downstream decrease in the velocity of a coastal current contained in the light upper layer of the ocean. The quasi-geostrophic model consists of two piecewise uniform potential vorticity regions separated horizontally by a free interface ("front") which intersects the vertical coastal wall in a "nose" region. As time increases, the slope of the front increases in this region, and the magnitude of the downstream convergence also increases, according to a nonlinear long-wave theory. At the time when this theory becomes invalid, the calculation is continued by numerical integration of the "contour dynamical" equations. This shows a continuation of the increase of the slope of the front near the nose, provided the total geostrophic transport is nonzero. (The case of zero transport is also discussed.) As time increases, a plume forms near the nose of the front, thereby transporting coastal water to very large offshore distances. It is suggested that this effect is responsible for some of the cold water plumes which extend to large distances from the coast of California. The cause of the small finite *initial* convergence (not implicit in our simple model) is attributed to differential upwelling or to a current instability.

1. Introduction

The California "squirt" is an example of a very large offshore deflection of a coastal current [Mooers and Robinson (1984), Rienecker, *et al.* (1985), Davis (1985), Flament *et al.* (1985)]. This relatively cold plume appears in satellite imagery as a thin jet emanating from an upwelling region. Under what conditions will the ubiquitous coastal disturbances evolve to such proportions?

1. Graduate School of Oceanography, University of Rhode Island, Narragansett, Rhode Island, 02882, U.S.A.

Spatially varying winds and topography provide one mechanism for downstream variations in the upwelled coastal current, and in the geostrophically adjusted regime. A description of this large problem in coastal oceanography is beyond the scope of this paper, and we will only consider the subsequent evolution of a slow downstream variation ("weak convergence") of the geostrophic current which may arise from the foregoing mechanism. Dynamic instability of a laminar coastal jet [Ikeda *et al.* (1984), Ikeda and Emery (1984)] provides another important mechanism for initiating disturbances and bringing them to finite amplitude. In this paper (as in Pratt and Stern (1986)) we try to isolate the dominant dynamics in the stage from large to very large disturbances (e.g., the squirt). Another important mechanism for the squirt effect is due to the presence of offshore geostrophic eddies [Davis (1985)]. The eddy/current interaction problem (to be dealt with in a subsequent paper) may result in the capture or entrainment of a portion of the currents, but in this paper we focus on an effect which is internal to the current.

The orientation of the sketch in Figure 1a may facilitate comparison with the California Current, the coast being on the right-hand side of the figure. The initial ($t = 0$) axis of the coastal current is indicated by the long-dashed curve which connects the points of maximum velocity at each x' section. M_o is the minimum distance of this axis from the coast, and the initial downstream velocity in the upper layer of the ocean is indicated by arrows. This layer has a mean thickness H and a density deficit $\Delta\rho$ relative to the much thicker and dynamically passive underlying layer. The Rossby radius of deformation, used as the horizontal length scale in the subsequent nondimensionalization is based on $\Delta\rho$, H, and the Coriolis parameter, and gravity. The maximum offshore extent of the initial axis is assumed to be of the order of the radius of deformation; and the Rossby number based on this width and the maximum velocity is assumed to be so small that the temporal evolution is quasi-geostrophic.

We will show that the weak initial ($t = 0$) downstream convergence in Figure 1a amplifies as faster portions of the coastal current "catch up" with slower ones, leading to a steepening of the current axis as indicated by that portion (Fig. 1a) drawn with a solid line. We believe that this simple model captures some important physical effects present in the ocean even though the Rossby number is larger, the baroclinic structure is more complex, and the topographic variations more explicit. The highly nonlinear geostrophic effects are by no means vitiated by the absence of Kelvin or other coastal waves in our model.

These conclusions will be based on the model in Figure 1b, which differs from Figure 1a in two respects. The upstream and downstream profiles in Figure 1b consist of piecewise uniform potential vorticity regions (with an artificial cusp in the downstream jet profile), and the maximum upstream current is at $y = 0$ (i.e., $M_o = 0$). The first of these simplifications eliminates current instability, according to the Rayleigh Theory which requires an extremum in potential vorticity for instability. The second simplification is a natural limiting case, and the other limiting case ($M_o \to \infty$ with $(L_o - M_o) = 0(1)$) corresponds to the free jet treated by Pratt and Stern (1986).
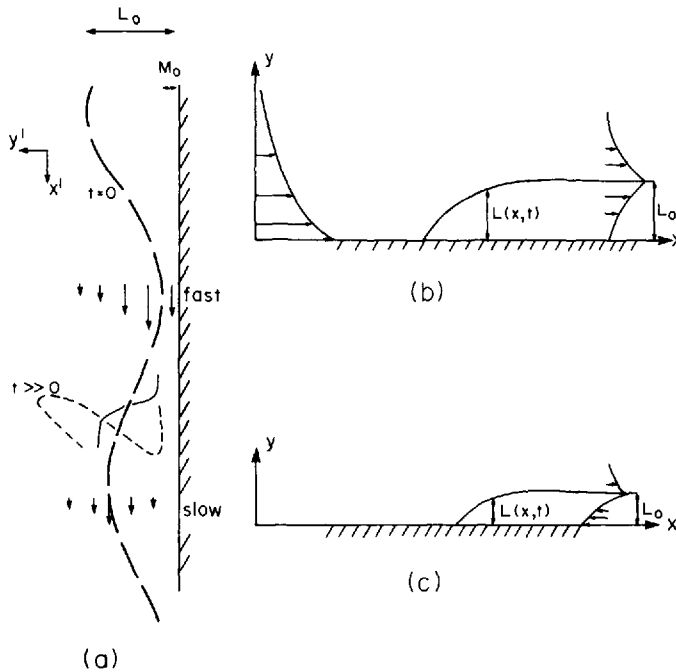
Figure 1. Schematic diagrams. (a) The dashed curve labeled $t = 0$ is the axis of a southward jet near the eastern boundary of a northern hemisphere ocean, and M_o is the minimum distance of the axis from the coast. The velocity arrows indicate a weak downstream convergence in the assumed initial state. As time increases, the axis steepens and folds, eventually $(t \gg 0)$ producing an offshore plume (or "squirt") of coastal water. (b) The model used to investigate the amplifying convergence when the maximum upstream current is at the coast $(M_o = 0)$. The fast current is now on the left and is x-independent far upstream, and the slower jet is x-independent far downstream. The current is modelled by two piecewise uniform potential vorticity regions, separated by an interface ("front") whose displacement from the coast is $L(x, t)$. The figure shows the upper and less dense layer of the ocean, and the lower layer is assumed to be relatively deep and motionless. (c) This model differs from the previous one in so far as there are no velocities at $x = -\infty$, and consequently the geostrophic velocity profile at $x = \infty$ has zero transport.

The piecewise uniform potential vorticity model in Figure 1c has zero velocity at $x = -\infty$, and thus the geostrophic current profile at all x has zero transport. We shall show that no squirt forms in this case, thereby identifying one condition necessary for squirts to form. This model (Fig. 1c) is also of interest for its own sake, and we shall compute the leftward propagation of the nose (n.b. if Kelvin waves were present, they would propagate energy to the right). This problem (Fig. 1c) reduces to the barotropic one of Stern and Pratt (1986) when the radius of deformation is much larger than the width of the coastal current.

For our "1½ layer" model the quasi-geostrophic dynamics takes the following form. Let $y = L(x, t)$ denote the nondimensional displacement (relative to the Rossby radius)

of the vorticity front from the wall ($y = 0$); let L_o denote the displacement at $x = \infty$; let $u(\infty, L_o, t)$ correspond to the velocity scale for the nondimensional x-velocity, let v denote the y-velocity, and let $Hh(x, y, t)$ denote the *departure* of the vertical layer thickness from its value at $y = \infty$. Then the normalized geostrophic potential vorticity vanishes at $y = \infty$ and in the entire region outside the front. If P_1 denotes the constant potential vorticity (Eq. 1.2) inside the front (Fig. 1b) then we have

$$u = -\partial h / \partial y \qquad v = \partial h / \partial x \tag{1.1}$$

$$\nabla^2 h - h = \begin{cases} 0, & y > L(x, t) \\ P_1, & y < L(x, t). \end{cases} \tag{1.2}$$

One boundary condition is $h(x, \infty, t) = 0$, and the wall boundary condition

$$v(x, o, t) = 0 \tag{1.3}$$

requires that $h(x, o, t)$ be constant.

If $L(x, t)$ is known at any time t, then (1.2) may be solved by decomposing its right-hand side into the sum of point potential vortices $P_1 dx dy$ of equal strength P_1. Each of these produces a circularly symmetric field h given by the Bessel function K_o. To satisfy (1.3) "image" vortices must be added. The resulting integral gives $h(x, y, t)$ from which $u(x, y, t)$, $v(x, y, t)$ are computed. By evaluating these on $y = L(x, t)$ we obtain the velocities dx/dt, dL/dt of any Lagrangian point on the front. From this $L(x, t + dt)$ can be computed, and by repetition of this process we obtain $L(x, t)$ at any time. Thus the introduction of the uniform potential vorticity profiles allows us to reduce the original problem containing two spatial dimensions to a one-dimensional problem, in which L is given as a solution of an integro-differential equation containing the aforementioned Green's function K_o. This contour dynamical method retains the full geostrophic nonlinearity (e.g., in dL/dt), and no artificial (eddy) viscosity is introduced.

2. The contour dynamical equations

First we note the far-field solution of (1.1 − 1.2) at $x = \infty$, where $L = L_o$ and $u(\infty, L_o, t) = 1$. For $y \geq L_o$ this solution is $u(\infty, y, t) = \exp -(y - L_o)$, and if A denotes an arbitrary constant then the solution inside the front is

$$u(\infty, y, t) = A \frac{\sinh y}{\sinh L_o} + (1 - A)e^{y - L_o}, (y < L_o). \tag{2.1}$$

Integration of this gives the wall height

$$h(\infty, o, t) = A \frac{\cosh L_o - 1}{\sinh L_o} + (1 - A)(1 - e^{-L_o}) + 1 \equiv P_2. \tag{2.2}$$

Two values of the free parameter P_2, corresponding to $A = (0, 1)$ will be considered,

and the $A \simeq 1$ case corresponds to a downstream jet (Fig. 1b) which vanishes at the wall. For all A the constant value P_1 of the potential vorticity inside the front equals the jump in *vorticity* across the front at $x = \infty$, and from (2.1) we see that A is related to P_1 by

$$P_1 = -\left(A \frac{\cosh L_o}{\sinh L_o} + (1 - A) + 1\right). \tag{2.3}$$

Next consider the flow far upstream ($x = -\infty$) in Figure 1b, where (1.3) implies

$$h(-\infty, o, t) = h(\infty, o, t) = P_2 \tag{2.4}$$

and therefore

$$u(-\infty, y, t) \equiv \bar{u}(y) = -\partial \bar{h}/\partial y = P_2 e^{-y} \tag{2.5}$$

where the bar denotes the upstream profile. When $P_2 = 0$ we obtain the zero transport case of Figure 1c.

It is convenient and illuminating to make the following formal separation. Let

$$u(x, y, t) = \bar{u}(y) + u'(x, y, t) \tag{2.6a}$$

$$h(x, y, t) = \bar{h}(y) + h'(x, y, t) \tag{2.6b}$$

$$u' = -\partial h'/\partial y. \tag{2.6c}$$

Since $\nabla^2 \bar{h} - \bar{h} = 0$ satisfies the same differential equation (1.2) as h, and since $h'(-\infty, y, t) = 0$, the appropriate Green's function for h' is $-(P_1/2\pi)K_o$. This Bessel function gives the circularly symmetric stream function produced by each area element $P_1 dx dy$ of potential vorticity on the right-hand side of (1.2). An image vortex $-P_1 dx dy$ must also be added (below the $y = 0$ plane) to satisfy the boundary condition (1.3), and the summation of all the vortices gives

$$h'(x, y, t) = \frac{-P_1}{2\pi} \int_{x_n(t)}^{\infty} d\xi \int_0^{L(\xi,t)}$$
$$d\eta \{K_o((x - \xi)^2 + (y - \eta)^2)^{1/2} - K_o((x - \xi)^2 + (y + \eta)^2)^{1/2}\} \tag{2.7}$$

where $x_n(t)$ is the nose point defined by $L(x_n(t), t) = 0$.

From (2.6c) we obtain

$$u'(x, y, t) = -\frac{P_1}{2\pi} \int d\xi \int_0^{L(\xi,t)} d\eta \left\{\frac{\partial}{\partial \eta} K_o(\ldots) + \frac{\partial}{\partial \eta} K_o(\ldots)\right\}$$

and evaluating this on the front $y = L(x, t)$ gives

$$u'(x, L(x, t), t) = \frac{-P_1}{2\pi} \int d\xi \{K_o((x - \xi)^2 + (L(x, t) - L(\xi, t))^2)^{1/2}$$
$$+ K_o((x - \xi)^2 + (L(x, t) + L(\xi, t))^2)^{1/2} - 2K_o((x - \xi)^2 + L^2(x, t))^{1/2}\}. \tag{2.8}$$

From $v = \partial h'/\partial x$ we also obtain

$$
\begin{aligned}
v = -\frac{P_1}{2\pi} \int d\xi \frac{\partial L(\xi, t)}{\partial \xi} \{K_o((x - \xi)^2 + (L(x, t) - L(\xi, t))^2)^{1/2} \\
-K_o((x - \xi)^2 + (L(x, t) + L(\xi, t)^2)^{1/2}\}.
\end{aligned}
\tag{2.9}
$$

It can be shown [Stern (1985)] that these expressions are still valid even if $L(x, t)$ is a multi-valued function of x, in which case the integrals are contour integrals, with $d\xi = (d\xi/ds)ds$ and ds is an element of arc length along the L-contour.

The Lagrangian integro-differential equation for material points $(x(t),L(x(t),t))$ on the front is then obtained from

$$
dL/dt = v
\tag{2.10}
$$

$$
dx/dt = u' + \bar{u}(L)
\tag{2.11}
$$

by substituting (2.9), (2.8), and the value of $\bar{u}(L)$ obtained from (2.5). Each point (x, L) on the front tends to move under the influence of two velocity components, one of which is the undisturbed upstream flow $\bar{u}(y = L)$. The other is the velocity (u', v) induced by all the anti-cyclonic potential vorticity *anomalies* located between the front and the wall.

3. Long-wave equations

We first consider the behavior of $L(x, t)$ when the variations in $L(x, 0)$ are large $(0(1))$ but slowly varying with x, i.e. L changes by a small fraction when x changes by $0(1)$. For $x \gg x_n$ the leading term in the long wave expansion of (2.9) is

$$
\begin{aligned}
v = -\frac{P_1}{2\pi}\frac{\partial L(x, t)}{\partial x} \int_{-\infty}^{+\infty} d\xi_1 \{K_o((\xi_1^2))^{1/2} - K_o(\xi_1^2 + (2L(x, t))^2)^{1/2}\} \\
= -\frac{P_1}{2}\frac{\partial L}{\partial x} (1 - e^{-2L})
\end{aligned}
\tag{3.1}
$$

where we have used the Bessel identity

$$
\frac{1}{\pi} \int_{-\infty}^{+\infty} d\xi \, K_o(\xi^2 + b^2)^{1/2} = e^{-|b|}.
\tag{3.2}
$$

The leading term in the expansion of (2.8) is

$$
u'(x, L, t) = -\frac{P_1}{2}\{1 + e^{-2L} - 2e^{-L}\}
$$

so that

$$
u(x, L, t) = P_2 e^{-L} - \frac{P_1}{2}\{1 + e^{-2L} - 2e^{-L}\}.
\tag{3.3}
$$

Substituting these in the kinematical condition

$$v = \frac{dL}{dt} = \frac{\partial L}{\partial t} + u\frac{\partial L}{\partial x} \tag{3.4}$$

gives

$$\frac{\partial L}{\partial t} + c(L)\frac{\partial L(x, t)}{\partial x} = 0 \tag{3.5}$$

where

$$c(L) = (P_2 + P_1)e^{-L} - P_1 e^{-2L}. \tag{3.6}$$

Eq. (3.5) is a first order hyperbolic equation whose well-known solution implies that each value of L propagates with a speed (3.6). If $\partial L(x, o)/\partial x \geq 0$, then steepening (increasing $\partial L/\partial x$ with time) will occur at those values of $L(x, o)$ for which $\partial c/\partial L = -(P_2 + P_1)e^{-L} + 2P_1 e^{-2L} < 0$. Referring to (2.2) we see that P_2 (the wall height) is positive $(0 < A < 1)$, and (2.3) shows that $P_1 < 0$, $-P_1 > P_2$ so that $\partial c/\partial L < 0$. We reach the important conclusion that steepening occurs continually in the region between the nose and $x = \infty$, until $\partial L/\partial x$ is so large that the long-wave theory fails. Although the foregoing asymptotic theory is not formally valid at the nose $(L = 0)$, we shall subsequently show that (3.6) also applies there as long as $\partial L/\partial x \ll 1$. This simple calculation verifies the introductory remarks (Sec. 1), viz that the fast coastal current (Fig. 1a) catches up to the slower part leading to a steeply sloping axis. We therefore direct our attention to the later stage times by considering the evolution of an arbitrary initial L which now has slopes of $0(1)$.

4. Coastal current with a finite transport

We shall now compute the contour dynamical solutions pertaining to two cases in which the relevant values of the constants are:

$$A = 0: \begin{cases} P_2 = 2 - e^{-L_o} & \text{(4.1a)} \\ P_1 = -2 & \text{(4.1b)} \\ u(\infty, y, t) = e^{y-L_o}, \, (y < L_o) & \text{(4.1c)} \end{cases}$$

$$A = 1: \begin{cases} P_2 = 1 + \dfrac{\cosh L_o - 1}{\sinh L_o} & \text{(4.2a)} \\ P_1 = -\dfrac{1 + \cosh L_o}{\sinh L_o} & \text{(4.2b)} \\ u(\infty, y, t) = \dfrac{\sinh y}{\sinh L_o}, \, (y < L_o), & \text{(4.2c)} \end{cases}$$

Explicit expression for the long-wave speed (3.6) can be obtained using the above values.

The speed u_n of the nose obtained by setting $L(x, t) = 0$ in (2.5) and (2.8) is

$$u_n = P_2 - \frac{2P_1}{2\pi} \int_{x_n}^{\infty} d\xi \, \{K_o((x - \xi)^2 + L^2(\xi, t))^{1/2} - K_o((x_n - \xi)^2)^{1/2}\}.$$

From now on x and $L(x, t)$ refer to distances measured in a coordinate system whose origin is fixed to the nose point, so that the above equation may be written as

$$u_n = P_2 + \frac{P_1}{2} - \frac{P_1}{\pi} \int_0^{\infty} d\xi \, K_o(\xi^2 + L^2(\xi, t))^{1/2}. \tag{4.3}$$

Let us note in passing that when L varies slowly with x at the nose then $L(\xi, t) \simeq 0$ in (4.3), which then gives $u_n = P_2$ in agreement with the *formal* limit of (3.6) as $L \rightarrow 0$. Thus (3.6) is valid at all L as previously asserted. In this limit the nose point moves with the maximum upstream velocity.

In the new moving coordinate system the equations of motion (2.10)–(2.11) are

$$\frac{dL}{dt} = \frac{-P_1}{2\pi} \int dL(\xi, t)\{K_o((x - \xi)^2 + (L(x, t) - L(\xi, t))^2)^{1/2}$$

$$- K_o((x - \xi)^2 + (L(x, t) + L(\xi, t))^2)^{1/2}\} \tag{4.4}$$

$$\frac{dx}{dt} = P_2(e^{-L} - 1) - \frac{P_1}{2} + \frac{P_1}{\pi} \int d\xi \, K_o(\xi^2 + L^2(\xi, t))^{1/2}$$

$$- \frac{P_1}{2\pi} \int d\xi \{K_o((x - \xi)^2 + (L(x, t) - L(\xi, t))^2)^{1/2} + K_o((x - \xi)^2$$

$$+ (L(x, t) + L(\xi, t))^2)^{1/2} - 2K_o((x - \xi)^2 + L^2(x, t))^{1/2}\} \tag{4.5}$$

where $d\xi \partial L / \partial \xi$ in (2.9) has been replaced by dL and the limits of the integrals have been deleted to remind the reader that these are contour integrals in general.

It will be helpful to compute analytically the *instantaneous* velocities for the step function:

$$L(x, o) = \begin{cases} 0, x < 0 \\ L_o, x > 0. \end{cases} \tag{4.6}$$

The nose velocity (4.3) is then

$$u_n = P_2 + \frac{P_1}{2} (1 - e^{-L_o}). \tag{4.7}$$

Relative to this the velocities $u = u^+$, $v = v^+$ at the "top" ($y = L_o$, $x = 0$) of the step, obtained from the right-hand side of (4.4) and (4.5), are

$$v^+ = -\frac{P_1}{2\pi} \int_0^{L_o} dL\{K_o((L_o - L)^2)^{1/2} - K_o((L_o + L)^2)^{1/2}\} > 0 \tag{4.8}$$

$$u^+ = P_2 (e^{-L_o} - 1) - \frac{P_1}{2} + \frac{P_1}{\pi} \int_0^\infty d\xi \, K_o(\xi^2 + L_o^2)^{1/2}$$

$$-\frac{P_1}{2\pi} \int_0^\infty d\xi \, \{K_o(\xi^2)^{1/2} + K_o(\xi^2 + (2L_o)^2)^{1/2} - 2K_o(\xi^2 + L_o^2)^{1/2}\}$$

$$= P_2(e^{-L_o} - 1) - \frac{3P_1}{4} + P_1 e^{-L_o} - \frac{P_1}{4}e^{-2L_o}. \quad (4.9)$$

When $A = 0$ (Eqs. 4.1) the nose velocity (4.7) is $u_n = 1$, $u(-\infty, o, t) = 2 - e^{-L_o}$, $u(\infty, o, t) = e^{-L_o}$, and (4.9) gives

$$u^+ = -\frac{1}{2} + e^{-L_o} - \frac{e^{-2L_o}}{2} < 0. \quad (4.10)$$

This means that the $x = 0$ edge of the initial step (4.6) will start to tilt backwards. Eq. (4.10) also implies that an initial state with single valued L but with a large positive $\partial L/\partial x$ will develop an even larger slope at a slightly later time and will then become multi-valued. When $A = 1$ we obtain $u^+ = -(1 - e^{-L_o})^2/2 < 0$, so that the same qualitative conclusion holds.

5. Numerical calculations

The numerical problem posed by (4.4)–(4.5) requires only a minor modification (due to the nose boundary condition) of contour dynamical programs used and tested in previous work [e.g., Stern (1986) and Stern and Pratt (1986)] and this may be consulted for the details of the numerical procedure. In brief, the method consists of distributing N Lagrangian points on the initial $L(x, o)$, and computing (4.4)–(4.5) by trapezoidal approximations to the integrals. These are indented at the logarithmic singularity of K_o, and an analytical approximation for this small region is used. Forward integration in time is accomplished by a second order Runge-Kutte approximation. As t increases, new Lagrangian points were inserted in the nose region in order to maintain adequate spatial resolution. When the first point downstream from $x = 0$, $L = 0$, exceeded a certain distance a new Lagrangian point was automatically inserted half-way in between. (We experimented with various values of this distance to convince ourselves of numerical stability and reproducibility.) With regard to the downstream boundary condition we note that the last integrand in (4.5) vanishes for large ξ when x is finite, i.e. $0 < x \ll x_N \rightarrow \infty$. Accordingly the integrals evaluated for $x \ll x_N$ were truncated at x_N. The last two points (i.e. x_N and x_{N-1}), on the other hand, were moved with the undisturbed velocity because their distance from the nose was sufficiently large.

All runs reported herein had an initial condition of the form

$$L(x, o) = L_o(1 - e^{-ax}). \quad (5.1)$$

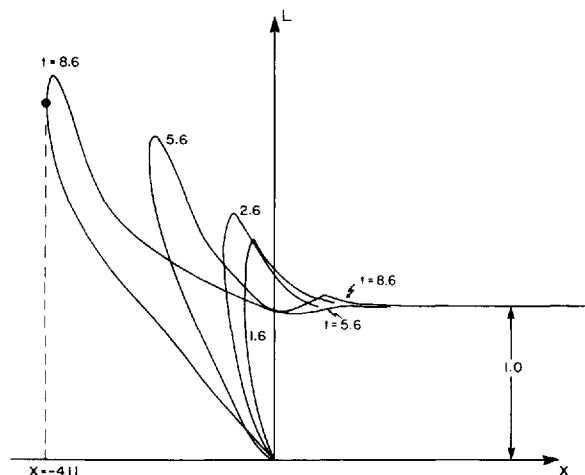The first run (Fig. 2) for $A = 0$, $a = 250$ was sufficiently close to the step function (4.6)

Figure 2. The temporal (t) evolution of Figure 1b when $L_o = 1$ (one radius of deformation), $A = 0$ (see text), and $a = 250$.

so that we were able to check the theoretical values of (4.8)–(4.9) against the numerical calculations of u^+, v^+ after one Runge-Kutte time step $\Delta t = 0.1$. As expected from (4.10), the steeply sloping nose tilts backward at the "early" time $t = 1.6$. The initial velocity $u_n = 1$ of the nose exceeds the mean velocity in $0 < y < L_o$ at $x = +\infty$, and thus there is a relative transport of water from the region inside ($y < L$) the front toward the nose. This accounts for the formation of the plume in Figure 2, and its continuation in Figure 3. At $t = 14.7$ the straining effect in the plume resulted in an excessively sparse distribution of points, and therefore the calculation was redone starting from $t = 9.7$ with some points deleted and some points added to improve the resolution. The new integration yielded the curve labeled $t = 14.7$(b) which overlapped the old calculation at $t = 14.7$ (not shown). Although the distribution of points is still not satisfactory to continue the calculation beyond $t = 14.7$, it is strongly suggested that the plume is about to detach from the rest of the front and to leave it behind. Although the problem posed by the long time $t \gg 14.7$ evolution is an interesting one, it is also delicate and beyond the resources (a personal computer) available to the author. Furthermore, in connection with plume detachment, one should recognize the intervention of smaller scale (e.g., eddy diffusion) processes in the prototype which will cut off the neck of the plume before the computer does (see Pratt and Stern (1986)). The evolution of the plume in Figure 4 is similar despite the fact that the initial nose was less blunt ($a = 1$).

For each of the two previous runs the nose speed was computed directly from (4.3), and also indirectly from the conservation of mass (or the conservation of area in the (x, y) plane for a quasi-geostrophic flow). This implies that the rate of increase of the area bounded by the front between $x = 0$ and $x_N(t)$ is equal to the relative flux at $x_N(t)$.
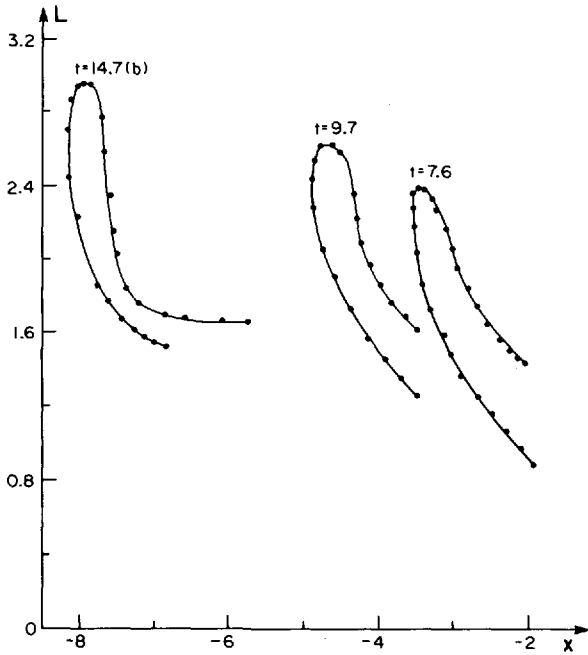
Figure 3. The temporal continuation of Figure 2 showing a portion of the plume up to a time when the distribution of Lagrangian points (the dots) has become too sparse to continue.
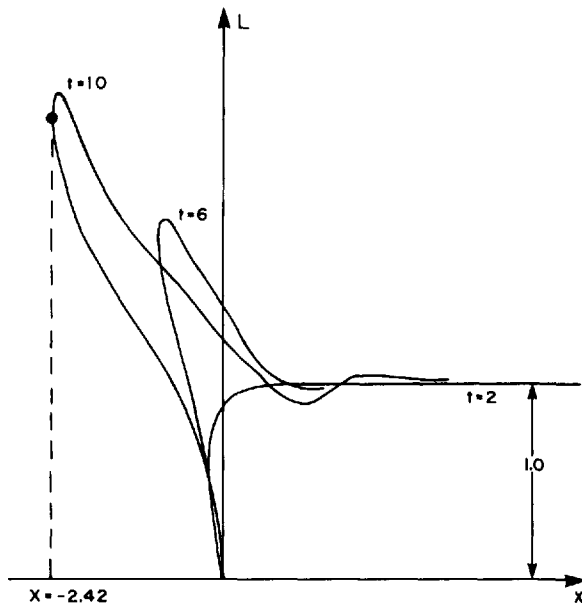

Figure 4. Same as Figure 2 except that $a = 1$ so that the initial nose is less blunt. But the nose still steepens and a plume still forms.
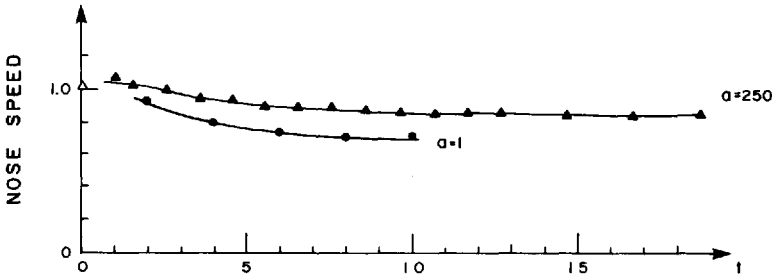
Figure 5. The nose speed as a function of time for the initial state of Figure 2 ($a = 250$) and Figure 4 ($a = 1$).

The later equals $-(u(\infty, y, t) - u_n(t))$ integrated from $y = 0$ to $y = L_o$, and the value of this is known except for $u_n(t)$. Thus the nose velocity can be computed by evaluating the area in $0 < x < x_N(t)$, and the curves in Figure 5 were obtained in this way. The "directly" measured u_n, on the other hand, had a much larger scatter ($\pm 10\%$) because (4.3) is sensitive to small fluctuations or errors in L near the nose [see Stern and Pratt (1985) for a similar problem at the nose of a barotropic intrusion]. But we have found, by varying the density of points and the time step, that the major structural properties (max$L$, min$L$, area) are very robust and reproducible. The calculation for $a = 1$ started with $N = 44$ Lagrangian points, and with the insertions at $x = 0$ the number reached $N = 86$ at $t = 10$.

The next calculation (Fig. 6) is for $A = 1$ which has a smaller value of $u(\infty, o, t)$, a slightly different $u(-\infty, o, t)$, and a more dense distribution of initial Lagrangian points which improves the resolution near the nose by a factor of two. The main difference between Figure 6 and Figure 4 is that the backward bending of the plume at $t = 6$ is less in the former case. Consequently the anti-cyclonic anomalies in the plume have a larger inductive effect at $x \sim 1$, which accounts for the trough in L at $t = 14$ and for the developing wave train in Figure 6. At $t = 20$ we see the plume about to pinch off at its neck. The Lagrangian point #59 was located at the nose at $t = 14$, and the point #33 was located at the nose at $t = 11.6$, implying an average offshore velocity of $3/(20-11.6)$ times the maximum jet velocity.

When L_o is doubled, other things being equal, a plume of greater area tends to form (Fig. 7). The Lagrangian point located at the maximum L when $t = 16$ had an average (from $t = 9.6$ to $t = 16$) offshore component of velocity equal to 0.5. On the other hand when L_o is halved (Fig. 8), the nose speed approaches the mean speed inside the front at $x = \infty$, leading to a plume of smaller volume and different character. The point #90 is moving toward $(-x)$ with a speed of 0.5 and is apparently about to cut off the plume at a much smaller value of y than in the previous cases. Point #70 was located at the nose at $t = 3.5$.

A link between the long wave analytical theory and the foregoing calculations is provided by Figure 9, which had the relatively small value of $a = \frac{1}{3}$ for its initial state.
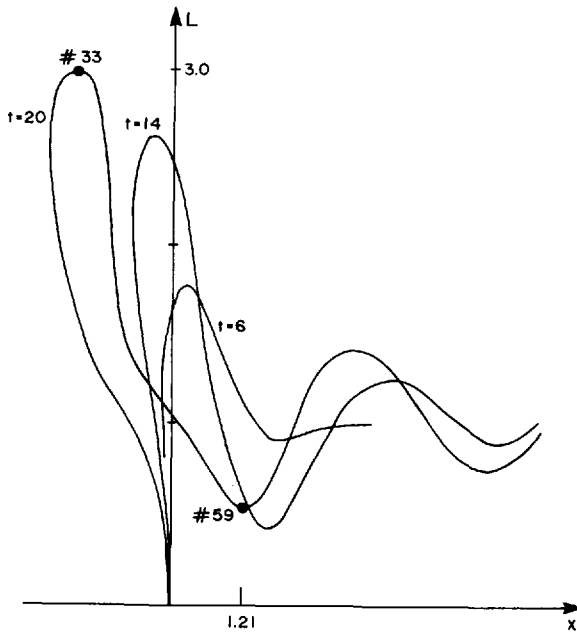
Figure 6. This has the same conditions as Figure 4 except that $A = 1$ ($u(\infty, o, t) = 0$), and also the initial density of Lagrangian points near the nose is greater.

At $t = 1$ the increase in L for $x \gg 0$ is in accord with the long wave theory, and the plume which forms later on is similar to that which occurred for the larger values of a. Figure 10 gives the directly computed (from Eq. 4.3) nose speed for three different L_o having the same values of a and A. Although these $u_n(t)$ may have 10% errors, for reasons mentioned previously, we may conclude from Figure 10 and Figure 5 that the
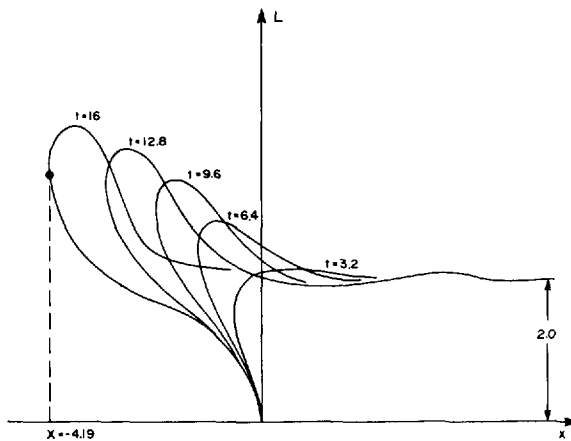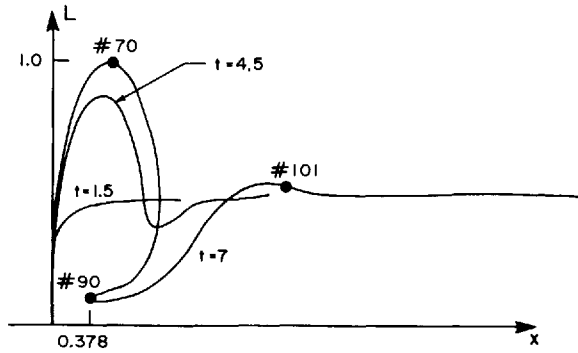

Figure 7. Same as Figure 6 except $L_o = 2$.

Figure 8. Same as Figure 6 except $L_o = .5$. For this small L_o the nose speed at $t = 4.5$ equals .48 and at $t = 7$, it equals .45.

nose speed decreases toward a value approximately equal to one half the maximum jet velocity.

6. The intrusive nose with zero transport

To obtain the equations of motion which correspond to Figure 1c in which $u(-\infty, y, t) = 0$ we merely set $P_2 = 0$ (Eq. 2.4), and this determines A. Then (2.3) determines P_1, and we may proceed with the solution of (4.4)–(4.5). However in that which follows the
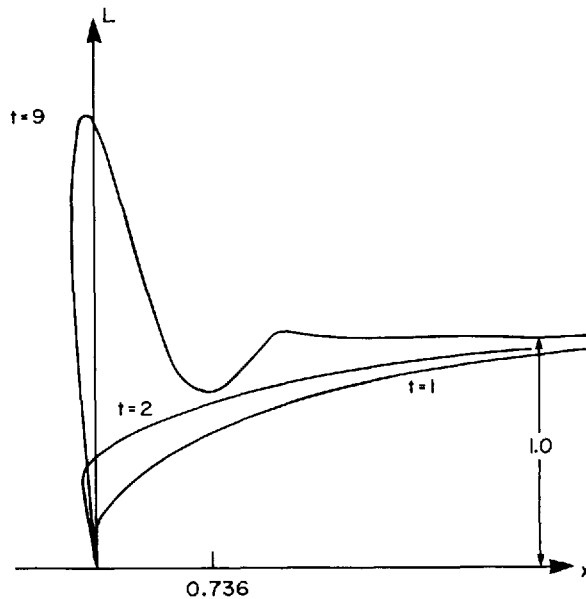

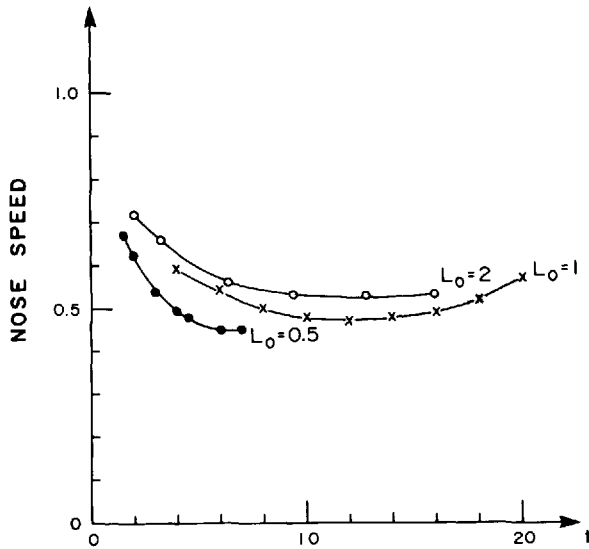Figure 9. Same as Figure 6 except $a = \frac{1}{3}$ (a weaker *initial* convergence).

Figure 10. Nose speeds computed from (4.3) for Figures 6, 7, 8.

unit of velocity (for the nondimensionalization) has been changed so as to make $u(\infty, o, t) = -1$.

Figure 11 shows the temporal evolution for $L_o = 1$ and for two different values of $a = 1$, $a = 2$. In both cases the initial slope at the nose increases up to about $t = 2$, after which a steady state L seems to be established at the nose. This is indicated by the three
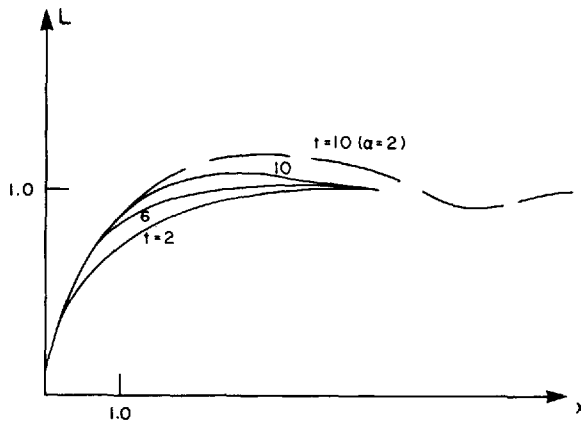

Figure 11. The "pure" intrusive case (Figure 1c) for $L_o = 1$, $a = 1$ at $t = 2, 6, 10$. Also shown at $t = 10$ is the case $a = 2$, $L_o = 1$, which indicates the evolution toward a *nose* shape $L(x, \infty)$ independent of initial shape.
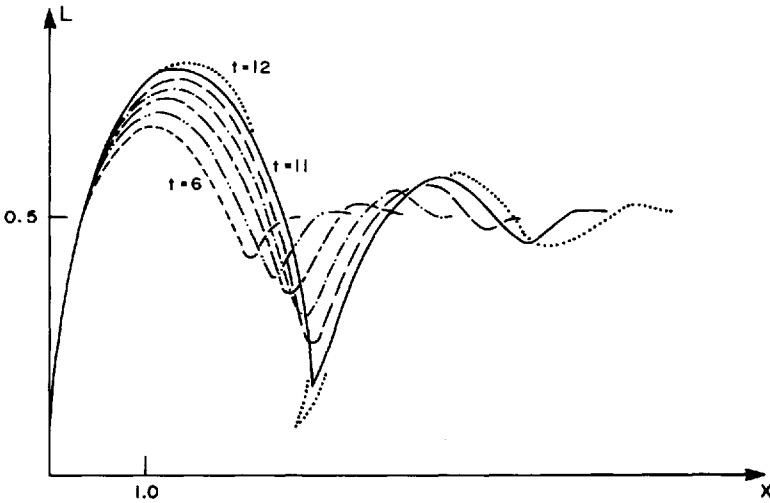
Figure 12. Same as Figure 11 except $L_o = .5$, $a = 1$. The curves from $t = 6$ to $t = 12$ are one unit apart in time. Note the cusp-like feature which forms at $t = 11$ and also appears in the dotted curve for $t = 12$ (only part of which is shown for the sake of clarity).

curves, $t = 2,6,10$ for $a = 1$ together with the $a = 2$ calculations for which only the result at $t = 10$ is shown in Figure 11. Apparently the equilibrium shape of the nose is independent of initial conditions (but it does depend on L_o and the radius of deformation). For $a = 2$ the nose velocities $u_n(t)$ at $t = 2,4,6,8,10$ are: $-.28$, $-.30$, $-.31$, $-.32$, respectively. For $a = 2$ the values of $u_n(t)$ at $t = 1,2,3,4,5,6,7,8,9,10$ are: $-.31$, $-.31$, $-.32$, $-.32$, $-.32$, $-.32$, $-.32$, $-.32$, $-.32$, $-.32$, respectively. If an exact steady state exists at the nose, then the (geostrophic) mass conservation requires $u_n = L_o^{-1} \int_0^{L_o} u(\infty, y, t)dy = -.32$ for $L_o = 1$. This agreement of the u_n values is a significant consistency result since mass conservation is not necessarily guaranteed by the *numerics*. We should point out however that an exact steady state has not yet been reached in Figure 11, and a small amplitude lee-wave seems to be slowly developing at $t > 10$.

The lee effect is much more pronounced in Figure 12 where L_o has been halved. Although some sort of steady similarity solution seems to be developing at the nose, and although $u_n(t)$ seems to have settled down to a steady value of $\approx -.46$ at $t = 12$, this u_n is significantly less than the theoretically required value of $-.40$ for an exact steady state. The discrepancy is due to the pronounced unsteadiness between the nose and $x = \infty$. The region in question (Fig. 12) at $t = 12$ is about to form a detached or cutoff anticyclonic eddy as the cusp-like minimum L heads for the wall. For smaller value of L_o our equations reduce to the barotropic ones studied by Stern and Pratt (1986), which reveal a qualitatively similar structure to that shown in Figure 12 for $L_o = .5$. Taken together the two papers cover a significant portion of parameter space, and

indicate the different evolutionary patterns of a convergent coastal current, depending upon its width, radius of deformation, and the ambient mean flow.

7. Discussion and conclusion

The following remarks may help to partially rationalize (or at least summarize) the squirt effect.

In the weakly convergent $(\partial L(x, o)/\partial x \ll 1)$ initial state (Fig. 1a,b) the upstream velocity at small y exceeds the downstream velocity, the pressure increases downstream on a line of constant y, and a kind of "blocking" high pressure region is presented to the upstream flow (Fig. 1b). It is relatively easy to see that in this state the nose point $L = 0$ moves with the fast upstream flow at $y = 0$, thereby overtaking the slower fluid downstream. The implied steepening of the nose of the front is consistent with that which is predicted for all L by the long-wave analytic theory. The image vortices and their mutual induction effect are crucial here, because when $M_o = \infty$ (the case of a *free* jet considered by Pratt and Stern (1986)) the propagation speed of long waves is zero and there is no steepening at this stage. As max $\partial L/\partial x$ increases (Fig. 1b), the offshore velocities increase, and therefore the downstream convergence must increase. Also L increases near the nose, u_n decreases (4.3), and more anti-cyclonic vortex anomalies come closer to nose. This increases the induced offshore velocities near the nose of the front, and the accumulation of anticyclonic vortices also tends to rotate the nose of the front in the opposite sense to that of the long-wave effect. These two effects can balance leading to an equilibration of the nose at a finite $\partial L/\partial x = 0(1)$ if, as occurs in Figures 11 and 12, there is *no* upstream flow. But in Figure 1b there is a *finite* $\bar{u}(L)$, and this must be added to the u' produced by the vortex anomalies. Since $\bar{u}(L)$ decreases with L, its effect is to rotate the nose of the front in the opposite sense to u', and (4.10) shows that the sum of all effects is to continue the steepening predicted by the long-wave theory. At this "blunt nosed" stage of development, the nose speed is approximately equal to the maximum jet velocity far downstream, and this speed exceeds the mean velocity from $y = 0$ to $y = L_o$. Consequently there is a relative mass transport from $x = +\infty$ toward the nose, thereby leading to the growth of the plume. Although the nose speed then starts to decrease (Fig. 5), it still will exceed the mean speed inside the front at $x = +\infty$, provided L_o is sufficiently large (Fig. 7). Thus the volume occupied by the plume increases with time and also increases with L_o. The contour dynamical calculations suggest that the plume pinches off and is left behind by the propagating front. But this stage of the process needs to be investigated further, and our limited time calculations by no means completes the story.

A change in the character of the plume occurs as L_o is decreased (Fig. 8). As the nose of the front steepens and as the maximum value of $L(x, t)$ starts to increase above L_o, the *anticyclonic* potential vorticity anomalies in the growing plume tend to induce shoreward displacements of the front at larger x. The close proximity of the coast $(L_o \to 0)$ causes the front to turn (as at $t = 7$ in Fig. 8) and to pinch off at a smaller

value of y and at an earlier time than occurs when L_o is larger. See Figure 23 in Pratt and Stern (1986) where the small L_o regime is more clearly isolated.

To relate our limited degree of freedom model to the ocean, we imagine the cold upwelled water in the latter case to be a relatively thin tracer, initially located very near the wall (Fig. 2), and on either side of the nose. This thin tracer is then advected toward the stagnation point from both sides of the nose, and then deflected offshore along the vorticity front. The cold water tracer may appear on the inside of our growing "plume" and also on the outside perimeter of the front. After (or near to) the time when the elongated plume detaches, it no longer is subject to the strong vortical constraints in the coastal current, so that the whole plume may be advected and entrained by an offshore eddy that happens to be in its vicinity [Simpson (1984)]. If so, the relatively small (baroclinic) energy of the plume will be added to the offshore eddy, perhaps helping to maintain these relatively slowly decaying systems.

The formation of a far reaching plume, according to the foregoing theory, depends on the existence of a nonzero transport in the convergent coastal current system. The calculations for zero transport bear this out, and this regime is also of interest because it shows how a coastal shear flow (with a potential vorticity gradient) can propagate into an otherwise resting region. Note that a Kelvin wave propagates energy in only one direction, and does not propagate gradients of potential vorticity, whereas the nose of the pure coastal intrusion can propagate potential vorticity in two opposite directions. When $L_o = 1$, the evolution shown in Figure 11 seems to be approaching a steady state relative to the nose, which propagates with a velocity $u_n \sim -.3$. Resting parcels lying ahead of the nose are therefore displaced seaward as the nose advances, and no plume forms. Even in Figure 12 no far-reaching plume can be said to form, but rather a pronounced frontal wave which leads to the (apparent) detachment of a near coastal eddy, and the formation of a new nose. The whole process may repeat and may be important for the formation of eddies in the near coastal regime.

REFERENCES

Davis, R. E. 1985. Drifter observations of coastal surface currents. J. Geophys. Res., *90,* 4741–4755.

Flament, P., L. Armi and L. Washburn. 1985. The evolving structure of an upwelling filament. J. Geophys. Res., *90,* 11,765–11,788.

Ikeda, M. and W. J. Emery. 1984. Satellite observations and meanders in the California current system off Oregon and northern California. J. Phys. Oceanogr., *14,* 1432–1450.

Ikeda, M., L. A. Mysak and W. J. Emery. 1984. Observations of satellite sensing meanders and eddies off Vancouver Island. J. Phys. Oceanogr., *14,* 3–21.

Mooers, C. N. K. and A. R. Robinson. 1984. Turbulent jets and eddies in the California Current and inferred cross-shore transports. Science, *223,* 51–53.

Pratt, L. J. and M. E. Stern. 1986. Dynamics of potential vorticity fronts, and eddy detachment. J. Phys. Oceanogr., *16,* 1099–1118.

Rienecker, M. M., C. N. K. Mooers, D. E. Hagan and A. R. Robinson. 1985. A cool sea surface anomaly off northern California. J. Geophys. Res., *90,* 4807–4818.

Simpson, J. J. 1984. An offshore eddy in the California current system. Prog. Oceanogr., *13*, 71–93.

Stern, M. E. 1985. Wave breaking and shingle formation in large-scale shear flow. J. Phys. Oceanogr., *15*, 1274–1283.

Stern, M. E. and L. J. Pratt. 1985. Dynamics of vorticity fronts. J. Fluid Mech., *161*, 513–532.